OCCLUSION OF THE LUMBAR SPINE CANAL DURING HIGH-RATE AXIAL COMPRESSION

Dale L. Robinson[a] , Kwong Ming Tse[a], Melanie Franklyn[b], David C. Ackland[a], Martin Richardson[c], Peter Vee Sin Lee[a]

[a]Department of Biomedical Engineering, University of Melbourne, Melbourne, Victoria, Australia

[b]Defence Science and Technology, Melbourne, Australia

[c]Department of Surgery, Epworth Healthcare, Melbourne Australia

Submitted as an original article to The Spine Journal

Word count: Text: 4,315 (Introduction to Clinical Significance), Abstract: 281.

25 October 2019

FUNDING DISCLOSURE STATEMENT: No competing financial interests exist.

ACKNOWLEDGEMENTS: Funding for this research was provided by Defence Science and Technology Group, Australia (MyIP 5818). Thanks to the Melbourne TrACEES Platform (Trace Analysis for Chemical, Earth and Environmental Sciences) for access to the GE phoenix nanotom m micro-CT scanner and technical support from Dr. Jay Black. We also acknowledge the facilities and scientific and technical assistance of the National Imaging Facility, a National Collaborative Research Infrastructure Strategy (NCRIS) capability, at Monash Biomedical Imaging, Monash University.

Corresponding author:

Peter Vee Sin Lee

Department of Biomedical Engineering

University of Melbourne, Victoria 3010, Australia

Abstract

Background context

While burst fracture is a well-known cause of spinal canal occlusion with dynamic, axial spinal compression, it is unclear how such loading mechanisms might cause occlusion without fracture.

Purpose

To determine how spinal canal occlusion during dynamic compression of the lumbar spine is differentially caused by fracture or mechanisms without fracture and to examine the influence of spinal level on occlusion.

Study design

A cadaveric biomechanical study.

Methods

Twenty sets of three-vertebrae specimens from all spinal levels between T12 and S1 were subjected to dynamic compression using a hydraulic loading apparatus up to a peak velocity between 0.1 and 0.9 m/s. The presence of canal occlusion was measured optically with a high-speed camera. This was repeated with incremental increases of 4% compressive strain until a vertebral fracture was detected using acoustic emission measurements and computed tomographic imaging.

Results

For axial compression without fracture, the peak occlusion (O_{max}) was 29.9±10.0%, which was deduced to be the result of posterior bulging of the intervertebral disc into the spinal canal. O_{max} correlated significantly with lumbar spinal level ($p<0.001$), the compressive displacement ($p<0.001$) and the cross-sectional area of the vertebra ($p=0.031$).

Conclusions

Spinal canal occlusion observed without vertebral fracture involves intervertebral disc bulging. The lower lumbar spine tended to be more severely occluded than more proximal levels.

Clinical Significance: Clinically, intermittent canal occlusion from disc bulging during dynamic compression may not show any radiographic features. The lower lumbar spine should be a focus of injury prevention intervention in cases of high-rate axial compression.

Keywords: Spinal canal occlusion, axial compression, lumbar spine, traumatic spinal cord injury

Introduction

Occlusion of the spinal canal resulting from high-energy trauma may lead to impingement of the spinal cord or nerves of the cauda equina, resulting in neurological deficits [1]. Retrospective surveys of traumatic spinal injuries have shown that the severity of neurological impairment is directly associated with spinal column fracture [2,3]. However, intervertebral disc bulging, which can result in neural compression, has received little attention to date [4–7]. Specifically, the spinal loads associated with level-specific disc occlusion of the canal are not known.

While the temporal characteristics of fracture-induced occlusion under high loading rates have been examined[8–11], fractures below the thoracolumbar junction and the relationship of spinal level to the degree of occlusion have not been previously considered. Spinal fractures below the thoracolumbar junction are proportionately more common with military compared to civilian injury. In a retrospective review of combat-related injuries, there was a high rate of burst fractures observed below L2 [12]. A recent text on military injury biomechanics reported that, for underbody blast attacks of military vehicles, the greatest proportion of spinal injuries was observed in the lumbar region [13].

Dynamic cadaveric tests have shown that a burst fracture of the vertebral body can occlude the spinal canal by up to 50% before reducing to approximately 30% due to the elastic response of the posterior longitudinal ligament or the intervertebral disc [9,11]. Previous studies have described canal occlusion to be the result of bone fragments derived from the fractured vertebral body protruding into the canal, with the maximum occlusion affected by the amount of compressive impact energy or loading rate [8–10,14]. In these studies, a burst fracture in three-vertebrae cadaveric specimens using a drop tower was produced. However, since disc protrusion could not be directly visualized during testing, the specific canal occlusion mechanism could not

be established.

Spinal canal occlusion associated with disc herniation in vivo has been measured with MRI [7,15–17], but these studies considered slow and non-injurious spine loading. Cuchanski et al., [4] measured the occlusion of fifteen sets of two-vertebrae spine specimens under compressive or bending loading conditions. While these authors considered specimens from multiple spinal levels (i.e., L1 to S1), the applied compression, bending moment and loading rate were of low magnitude (i.e., 250 N, 2.5 Nm and 0.01 Hz, respectively) which may not be sufficient to generate traumatic spine injury. Posterior protrusion of the intervertebral disc has been previously measured in static images of two-vertebra cadaveric specimen taken at different flexion/extension, lateral bending or axial rotation angles [5,6,18,19]. However, canal occlusion under dynamic compression in the absence of a severe vertebral fracture has not been measured in previous research.

Experimental studies of canal occlusion induced by vertebral fracture have primarily focused on the cervicothoracic and thoracolumbar junctions [8–11] since these are common fracture sites clinically encountered in civilian trauma [2,3]. However, morphometric variation along the spine is associated with changes in canal geometry [20,21], and it is unclear if these anatomical variations influence canal occlusion susceptibility. The aim of this study was to quantify how fracture and non-fracture trauma resulting from dynamic compression, or vertebral size, volumetric bone mineral density (vBMD) and lumbar position influence occlusion of the spinal canal during dynamic compression. It was hypothesized that fracture and the aforementioned variations between vertebrae influence the amount of occlusion.

Methods

Ethical approval for this study was obtained from the University of Melbourne Human Ethics

Committee (IDs: 1647558 and 1544171). The study was funded by Defence Science and Technology, Australia.

Specimen preparation

Vertebral columns extending from T12 to S1 inclusive were harvested from fifteen fresh-frozen male cadavers (age: 61.5±10.3 years, weight: 83.1±26.1 kg, height: 177.6±10.3 cm, BMI: 26.3±8.6 kg/cm^2; each expressed as mean±1SD). Spinal specimens showed no history of previous surgery and were free of macroscopic abnormalities, including bridging osteophytes or wedge deformities. All specimens were separated into twenty sets of three-vertebrae specimens comprising three-adjacent vertebra from all spinal levels between T12 and S1 (Table 1). All facet joints and associated capsular ligaments were left intact, as were the intervertebral discs and major spinal ligaments including the anterior longitudinal ligament, posterior longitudinal ligament, ligamentum flavum, intertransverse ligament, interspinous ligament and supraspinous ligament, facet capsular ligaments. All other soft tissues were removed. Specimens were kept hydrated by regular irrigation with 0.9% saline during preparation and testing.

Imaging

Each vertebral specimen was imaged in a small animal computed-tomography (CT) scanner (Inveon; Siemens, Munich, Germany), where the axial slice thickness and in-plane voxel size were each 0.1 mm. The three-dimensional bony geometry of each specimen was segmented using commercially available software (Mimics version 19.0; Materialise, Leuven, Belgium). Parameters measured directly from the reconstructed geometries included cross-sectional area at the mid-plane of each vertebral body of the center vertebrae (a_{VB}), cross-sectional area at the mid-plane of the lower intervertebral disc (a_{IVD}), height of the vertebral body of the center vertebrae

(h_{VB}), and height of the vertebral body of the center vertebrae and the lower intervertebral disc (h_{VB+IVD}) (Fig. 1). The CT images were used to identify Schmorls nodes or disc herniation into the endplate, and the most severely degraded disc for each specimen was graded according to clinical radiographic criteria [22]. The volumetric BMD (vBMD) of trabecular bone was determined for the center vertebral body using previously published methods [23].

Mechanical testing

The cranial and caudal vertebrae of each three-vertebrae specimen were embedded in an aluminum fixture using dental plaster with the vertebral rims of the center vertebra positioned horizontally, and the upper and lower vertebrae remained in their neutral position (i.e., unloaded) (Fig. 2). To enhance fixation, four metal screws were drilled into the outer vertebral bodies and steel wires tightly wound between each screw head prior to potting. The potted spine and fixtures were subsequently secured to a calibrated material testing machine (Model 8874; Instron, Norwood, USA), comprising a six degree-of-freedom load cell (MC5-2500; AMTI, Watertown, USA) mounted below a hydraulically-driven piston (Fig. 2). The vertical component of the force and the piston displacement represented the axial spine compressive force (F_z) and displacement (d_z), respectively. Using adjustment plates, the position of the potted spine was adjusted to ensure a 500 N pure axial compressive load, which was defined by measurement of flexion-extension and lateral bending moments of less than 1 Nm. Axial strain (ε_z) was calculated relative to h_{VB+IVD} as:

$$\varepsilon_z = \frac{d_{z,max}}{h_{VB+IVD}} \quad (1)$$

From an unloaded position, each spinal specimen was tested in a loading sequence (Fig. 2) that comprised (i) preloading: 5 cycles at 1 Hz from 0 to 0.1 mm of compression, (ii) dynamic loading: compression at maximum acceleration of the testing machine (i.e., peak velocity 0.1-0.9

m/s) to a 4% interval of ε_z, (iii) unloading: returning the spine to its unloaded position in 1 s, and (iv) recovery: maintaining the specimen in an unloaded position for approximately 30 minutes. The entire loading sequence was repeated in increments of 4% increase in ε_z until a fracture was detected by a visible crack on the left or right surface of the center vertebral body, or a negative slope in the force-displacement curve [24]. After testing, each specimen was removed from the testing machine and visually examined for damage to ligaments, discs and cortical bone.

Fracture identification

Fracture resulting from the final test in the series was evaluated by post-test CT images acquired of the center vertebra and classified according to the AO spine injury classification system [25]. To identify any vertebral body fractures that had occurred prior to the final test, two miniature acoustic emission (AE) sensors (S9225; Physical Acoustics Corp., Mistras Group, Princeton Junction, USA) were attached to the body of the center vertebra of each cadaveric specimen (Fig. 3), as described previously [26]. Briefly, the AE sensors were attached to the body of the center vertebra by smoothing a small region of the bony surface with a scalpel and sandpaper, degreasing the surface with ethanol, filling surface pores and water proofing with polyurethane, and bonding the sensor with cyanoacrylate glue. The AE signals were recorded using a data acquisition system with a sampling frequency of 2 MHz (USB-6366; National Instruments Corp., Austin, USA), and were converted to absolute AE sound wave pressure using the sensitivity curve supplied by the manufacturer for each sensor. It has been shown that if the duration of an AE burst ($AE_{duration}$) defined by a discrete period of AE activity greater than background noise is greater than 0.63 ms, the vertebral body has sustained an isolated trabecular fracture or a combined fracture of the cortical and trabecular bone [26].

Occlusion evaluation

Occlusion of the spinal canal was measured during testing using a pair of 45-degree mirrors that reflected a cold light source (LG-PS2-5; Olympus, Tokyo, Japan) downwards through the canal to a high-speed camera (Fastcam-3 or AX50; Photron, Tokyo, Japan) (Fig. 3). The images were sampled at 2,000 frames per second. Canal occlusion (O_{canal}) during the test was calculated from the decrease in illuminated canal area relative to the initial illumination area using:

$$O_{canal} = \frac{a_{canal} - a_{canal,i}}{a_{canal,i}} \quad (2)$$

where $a_{canal,i}$ is the initial canal area (in pixels) and a_{canal} represents the current canal area. The maximum occlusion (O_{max}) and corresponding compressive displacement ($d_{z,max}$) and force ($F_{z,max}$) were identified, whilst the final occlusion (O_{final}) was assumed to be the occlusion two seconds from commencement of compressive load (Fig. 4). The compressive strain at maximum occlusion ($\varepsilon_{z,max}$) was calculated as:

$$\varepsilon_{z,max} = \frac{d_{z,max}}{h_{VB+IVD}} \quad (3)$$

The timing of the load cell, acoustic emission signals and high-speed camera images was aligned with a digital trigger generated by the USB-6366 data acquisition system. The accuracy of this optical system was evaluated by comparing its occlusion measurements on a 3D-printed three-vertebrae polymer spine to those obtained using a motion capture system with four cameras (vero 2.2; Vicon, Oxford, UK) (see Supplementary material, part I). The root-mean-squared difference between each method was 5.49% and the coefficient of determination (R^2) was 0.946, which was assumed a satisfactory accuracy to validate the optical based method.

Data analysis

The temporal relationship between occlusion and the compression attributes, d_z and F_z, was

quantified using Pearson's correlation-coefficient (R), calculated from the start of compression to maximum occlusion ($t_{max,O}$). The strength of correlation was defined as either poor = 0-0.29; fair = 0.30-0.59; moderate = 0.60-0.79 or strong = 0.80-1.00 [27]. To avoid any bias resulting from different numbers of compression tests between specimens, only the second-last and final tests were considered in the analysis. These specific tests were chosen because they generated the greatest extent of canal occlusion per specimen. Based on the post-test CT images or $AE_{duration}$, these tests were designated as non-fracture or fracture, which was represented by the categorical variable fracture status, denoted as 0.0 and 1.0, respectively.

Independent stepwise multiple linear regressions were performed with the dependent variables O_{max} or O_{final}, and the independent predictor variables: Lumbar level, $d_{z,max}$, $\varepsilon_{z,max}$, a_{VB}, a_{IVD}, $a_{canal,i}$, h_{VB}, h_{VB+IVD}, vBMD, fracture status, Schmorl's nodes and intervertebral disc grading. This stepwise approach sequentially included predictors if the corresponding fit of the regression was significantly improved according to a partial F-test, whilst predictors that do not satisfy this criterion at any point in the regression were eliminated. The significance of the final regression was also assessed using an F-test. The level of significance for all analyses was set as $p<0.05$. Normality of the residuals was evaluated using a Kolmogrov-Smirnov test, and homoscedasticity of the residuals examined from a scatterplot of the standardized residuals and predictors. Absence of multicollinearity between explanatory variables was determined using variance inflation factors (VIFs).

Results

All fractures identified in the current study were confined to the vertebral body, and no specimen sustained ligament rupture or damage to the intervertebral disc upon visual inspection

and post-test dissection of the discs. The final test in each load series resulted in a fracture for all specimens, except two which did not have any detectable injury in their CT scans and were classified as non-fracture. The second-last test for 17 specimens was classified as non-fracture, whilst the second-last test for 3 specimens was excluded from the data analysis due to image acquisition issues with the high-speed camera. Thirteen specimens were identified to have a combined cortical and trabecular fracture, comprising cranial endplate fracture (n=3), split coronal fracture (n=6), incomplete burst fracture (n=4), while five specimen were identified with isolated trabecular fracture. For disc degradation, seven specimens were graded as 0 (normal), seven as 1 (mild) and six as 2 (moderate), and 0 as 3 (severe); however, no specimens had herniation of the disc into the endplate. Eight specimens were found to have pre-existing Schmorls nodes, indicating that the condition of the nucleus may have influenced the nature of the fracture sustained. Since most specimens had tests represented in both of the non-fracture and fracture groups, no attributes describing the vertebral body and canal size, vBMD and intervertebral disc grading varied significantly between non-fracture and fracture ($p>0.05$; Table 2).

The canal occlusion of each specimen closely followed the temporal measurements of compressive force and displacement (Fig. 5). Evaluated across all lumbar levels, the correlation up to the maximum occlusion between O_{canal} and d_z was strong, with an average R of 0.93 and 0.95 for non-fracture and fracture, respectively (Table 3). Over the same interval, the average R between canal occlusion O_{canal} and F_z was lower, with R values of 0.78 and 0.93 for non-fracture and fracture, respectively. When computed over the entire two seconds of testing, the R value computed between O_{canal} and d_z or F_z was on average weaker than the R value of the shorter interval (O_{canal} vs d_z: 0.86 and 0.83, for non-fracture and fracture, respectively) and (O_{canal} vs F_z: 0.83 and 0.71, for non-fracture and fracture, respectively).

Computed for all lumbar levels, O_{max} was not significantly different between the compression tests of non-fracture and fracture (Table 4); however, for every test the occlusion immediately reduced following O_{max} (Fig. 5), and O_{final} for non-fracture was significantly lower than for fracture (mean difference: 17.0%; p=0.011). $d_{z,max}$ and $\varepsilon_{z,max}$ for fracture were each significantly larger than for non-fracture (mean difference: 2.18 mm; p<0.001). At individual lumbar levels, O_{final} varied significantly between non-fracture and fracture at L4 (mean difference: 77.2%; p=0.011), whilst $d_{z,max}$ varied significantly between non-fracture and fracture at L5 (mean difference: 1.10 mm; p=0.011). No occlusion or compression variables were observed to vary significantly (p>0.05) between tests identified with isolated trabecular fractures or combined cortical and trabecular fractures (Table 5).

The stepwise linear regression for the dependent variable O_{max} produced a strong fit (R=0.822), with significantly correlated variables that included lumbar level and $d_{z,max}$ (p<0.001) and a_{VB} (p=0.031) (Table 6). O_{max} did not appear to depend upon the fracture status of the compression test (p>0.05). In contrast, the dependent variable O_{final} significantly varied with fracture status (p=0.026), albeit with a fair fit for the linear regression (R=0.37). Neither O_{max} or O_{final} was significantly affected by the presence of Schmorl's nodes or the intervertebral disc grading (each p>0.05). For each linear regression the corresponding residuals were found to be normally distributed, whilst the magnitude of the normalized predictors and residuals was less than three and their corresponding scatter plot was approximately rectangular; features that were each indicative of homoscedasticity. For the linear regression corresponding to O_{max}, the VIFs were less than 2.5, indicating there was no collinearity between each predictor.

Discussion

Occlusion of the spinal canal from mechanisms other than vertebral fracture present a clinical challenge since the injury may not present radiographically [28–30]. The results of this study demonstrate that substantial spinal canal occlusion may result from non-fracture mechanisms during dynamic spinal compression. For example, the maximum occlusion for non-fracture tests was 43.6±34.6% of the axial view of the unloaded canal area (Table 6). Since there was no bone damage identified for the specimens of the non-fracture group, the canal occlusion was likely due to mechanisms associated with soft tissue deformation, such as bulging of the intervertebral discs. While transverse dislocation or rotation of the center vertebra may have also caused occlusion, its contribution was likely minimal due to the confinement of the cranial and caudal facet joints [31], especially with the outer vertebra being clamped by dental plaster in the mechanical testing.

Up to peak occlusion (O_{max}), the temporal occlusion measurements most strongly correlated with the compressive displacement for tests corresponding to both fracture (R=0.93±0.13; p<0.001) and non-fracture (R=0.95±0.04; p<0.001) (Table 3), indicating that the amount of canal occlusion was proportional to the magnitude of axial compression. This relationship also supports a disc bulging occlusal mechanism, since experimental and computational studies have shown that radial disc bulging is proportional to compressive displacement [32,33]. The correlations between occlusion and compressive displacement remained significant over the entire two second interval of the axial compression, albeit with weaker correlations than the shorter interval (Table 3). This indicates canal occlusion over longer durations is influenced by other variables, likely relating to intervertebral discs viscoelasticity, which has a greater effect on the disc response across longer intervals [34,35]. O_{final} varied significantly between non-fracture and fracture across all lumbar spine levels (p=0.011; Table 4). This result suggests that, for the observed range of vertebral body

fractures associated with spinal compression, the spinal canal will experience prolonged occlusion compared to spinal compression without a fracture.

Stepwise regression indicated that O_{max} was significantly dependent on lumbar level ($p<0.001$), $d_{z,max}$ ($p<0.001$), and the vertebral body cross-sectional area (a_{VB}) ($p=0.031$), whilst the fracture status had no significant bearing on O_{max} (Table 6). The dependency between O_{max} and lumbar level is a novel result and suggests that more caudal lumbar canal levels have a greater tendency to be maximally occluded than levels more cranially. This result may be related to differences in the canal cross-sectional area, which was greatest at T12 and lowest at L5 (Table 2), or the dependency to a_{VB}, since vertebrae and adjoining discs with smaller cross-sectional areas will have a reduced compressive stiffness and therefore sustain greater disc compression causing bulge. This finding implies that occlusion-induced neurological injuries should be protected against for the lower lumbar spine since this region is more readily occluded during high rate axial compressions generated from falls or underbody blast attacks of military vehicles. However, this interpretation still requires clinical evidence linking neurological injuries to a disc bulging mechanism in both civilian and combat scenarios.

Schmorl's nodes were present in eight specimens and the intervertebral disc grading varied from normal to moderately degraded, however, this extent of disc degeneration had no significant effect ($p>0.05$) on O_{max} or O_{final} according to the stepwise regression (Table 6). While degeneration of the disc may be expected to influence disc bulging due to disruption of the annulus fibrosis lamellae [36], our results are consistent to previous work showing that the degeneration does not significantly change posterior bulging of the disc during axial compression [15,37]. As outlined by O'Connell et al. [37], this result may relate to the lower tensile moduli and less organized lamellae that occur in the posterior annulus fibrosis compared to those anteriorly [38,39].

The present study showed that O_{max} for the T12-L1-L2 specimens of the fracture group (26.6±10.4%; Table 4) was lower than that reported for dynamic compression of three-vertebrae specimens at the thoracolumbar junction (47.62±13.89% [10]; 33.3±10.6% [40]; 47.0±12.0% for impact energy of 110 J [14]). This discrepancy may be due to dissimilar loading protocols and fracture types, where these previous studies each used a drop-weight loading method and only considered burst fractures, whereas the current study used a hydraulic loading apparatus, which avoided overloading a specimen following fracture initiation, and considered compression fractures other than burst. For both non-fracture and fracture compressive tests, the magnitude of occlusion significantly reduced following its peak value (Table 4), a finding that was consistent with previous dynamic occlusion measurements [10,14,40]. Many studies have obtained occlusion measurements of the lumbar spine due to disc bulging from both cadaveric specimens [4] and in vivo [7,15–17], however, due to the low speeds and lower amounts of compression, the occlusion magnitudes were much lower than the current study.

This study had limitations that ought to be acknowledged. Firstly, by applying the incremental loading method, none of the fracture types included a complete burst fracture, which is the typical vertebral fracture type associated with canal occlusion and spinal cord injury [1,9]. The absence of burst fractures in the current study may be explained by the peak velocities in the mechanical testing (range: 0.1-0.9 m/s), which were lower than previous studies that produced these fractures during high-rate axial compression of the spine, where peak velocities were reported from 2.5 to 9 m/s [41,42]. However, burst fractures have also been reported to occur at force rates of 250 kN/s [10], which is comparable to the current study, where the average $F_{z,max}$ (non-fracture group: 4866.1 N, fracture group: 6261.2 N) and average time-to-peak force (non-fracture group: 18.5 ms and fracture group: 14.3 ms), corresponded to a force rate of 263.0 kN/s and 437.8 kN/s, for the

non-fracture group and fracture group, respectively. Hence, we would argue that the loading rate for the fracture group may have been sufficient to cause burst fracture. Another explanation is that the lack of burst fracture was related to the incremental loading approach, which initiated fractures but most likely prevented them from progressing into a complete burst fracture. This deduction is supported by the observed fracture patterns, where four specimens sustained an incomplete burst fracture, which may have progressed to a complete burst fracture with further compression, and three specimens sustained a cranial endplate fracture, which is believed to initiate the burst fracture process [43]. It is also worth noting that experimental studies have shown the mechanical behavior of the intervertebral discs becomes rate independent for stress rates greater than 1 MPa/s [34], which for the average a_{IVD} in the current study, equates to 2.2 kN/s; hence, occlusion measurements due to the disc bulging mechanism would not have changed at higher loading rates.

Secondly, the axial view of the spinal canal did not allow the relative contribution to canal occlusion by disc bulging or lateral vertebra motion to be visualized. However, the confinement provided by the clamped outer vertebra and facet joints likely minimized lateral motion of the center vertebra, a deduction supported by measurements from a second high-speed camera that was used to image two of the spinal specimens from an oblique sagittal viewing position (see Supplementary material, part II). Although deformation of the vertebral body may have contributed to canal occlusion, this effect was considered negligible due to the much greater stiffness of the bone compared to the discs [44,45]. This reasoning was supported from observations for two specimens viewed from the oblique sagittal viewing position, where the vertebral body displacement was minimal compared to that of the upper and lower intervertebral discs (see Supplementary material, part III).

Thirdly, while the optical-based occlusion measurements were validated for a rigid 3D-printed

polymer spine, differences from the cadaveric spine, such as variation in the spinal canal geometry, may have altered this accuracy. To further consider these geometric variations, the curvature of the spinal canal was measured in each cadaveric specimen and compared to the 3D-printed spine used to validate the occlusion measurements (see Supplementary material, part IV). It was found that the spinal canal curvature for specimens above L4-L5-S1 was similar to the 3D-printed spine and, thus, would be expected to provide occlusion measurements of similar accuracy. For the L4-L5-S1 specimens, the variation in the spinal canal orientation from a straight vertical line was approximately double that of the 3D-printed spine, thus, larger errors in the occlusion measurement would have occurred at this level and caution is advised when interpreting the current results pertaining to this lumbar level. Additional measurement errors would also have been dependent on the alignment of specimens in the loading apparatus, where the vertebral rims of the center vertebra were positioned horizontally to provide a vertical line-of-sight through the canal. By using a spirit level to guide the alignment, it would be expected that these errors would be relatively minimal compared to the errors related to the spinal curvature.

Finally, the imposed boundary conditions used in the mechanical testing may differ from those of the lumbar column during loading *in vivo*, where the curvature and compliance along the spine allows individual vertebra to translate and rotate during dynamic compression [46]. This may ultimately reduce posterior disc bulging toward the canal [47–50], resulting in possible overestimates of occlusion. However, this study limitation was unavoidable considering that level-specific occlusion under dynamic compression can only be measured in short spinal specimens at each lumbar level, each which has a reduced compliance compared to a full-length spine. Furthermore, the axial confinement was necessary to maintain the spinal canal within the line-of-sight of the light source and camera system used in the current study. Thus, using alternative

sensors such as pressure transducers is recommended in future work examining dynamic spinal occlusion corresponding with reduced axial confinement of the spine [42].

Clinical Significance

The present study showed that the spinal canal experiences considerable amounts of occlusion without vertebral fracture under dynamic compression, which is likely to be due to disc bulging. This finding is of relevance when considering imaging methods to identify potential spinal injury, since without vertebral fracture the spinal injury may not present any identifiable features in radiographic imaging. Caudal lumbar vertebrae were found to be more prone to occlusion than proximal lumbar vertebrae during axial compression, most likely due to variations in the canal and intervertebral disc cross-sectional area and load response. These findings suggest that the lower lumbar spine ought to be a focus for injury prevention in scenarios that produce dynamic spinal compression.

References

[1] Mattucci, S., Speidel, J., Liu, J., Kwon, B. K., Tetzlaff, W., and Oxland, T. R., 2018, "Basic Biomechanics of Spinal Cord Injury — How Injuries Happen in People and How Animal Models Have Informed Our Understanding," Clin. Biomech., **64**, pp. 58–68.

[2] Pickett, G. E., Campos-Benitez, M., Keller, J. L., and Duggal, N., 2006, "Epidemiology of Traumatic Spinal Cord Injury in Canada," Spine (Phila. Pa. 1976)., **31**(7), pp. 799–805.

[3] Leucht, P., Fischer, K., Muhr, G., and Mueller, E. J., 2009, "Epidemiology of Traumatic Spine Fractures," Injury, **40**(2), pp. 166–172.

[4] Cuchanski, M., Cook, D., Whiting, D. M., and Cheng, B. C., 2011, "Measurement of Occlusion of the Spinal Canal and Intervertebral Foramen by Intervertebral Disc Bulge," SAS J., **5**(1), pp. 9–15.

[5] Adams, M. A., and Hutton, W. C., 1982, "Prolapsed Intervertebral Disc: A Hyperflexion

Injury," Spine (Phila. Pa. 1976)., **7**(3), pp. 184–191.

[6] Adams, M. a, Dolan, P., and Hutton, W. C., 1988, "The Lumbar Spine in Backward Bending.," Spine (Phila. Pa. 1976)., **13**(9), pp. 1019–1026.

[7] Fredericson, M., Lee, S. U., Welsh, J., Butts, K., Norbash, A., and Carragee, E. J., 2001, "Changes in Posterior Disc Bulging and Intervertebral Foraminal Size Associated with Flexion-Extension Movement: A Comparison between L4-5 and L5-S1 Levels in Normal Subjects," Spine J., **1**(1), pp. 10–17.

[8] Ching, R. P., Watson, N. A., Carter, J. W., and Tencer, A. F., 1997, "The Effect of Post-Injury Spinal Position on Canal Occlusion in a Cervical Spine Burst Fracture Model," Spine (Phila. Pa. 1976)., **22**(15), pp. 1710–1715.

[9] Panjabi, M. M., Kifune, M., Wen, L., Arand, M., Oxland, T. R., Lin, R. M., Yoon, W. S., and Vasavada, a, 1995, "Dynamic Canal Encroachment during Thoracolumbar Burst Fractures.," J. Spinal Disord., **8**(1), pp. 39–48.

[10] Tran, N. T., Watson, N. A., Tencer, A. F., Ching, R. P., and Anderson, P. A., 1995, "Mechanism of the Burst Fracture in the Thoracolumbar Spine. The Effect of Loading Rate," Spine (Phila. Pa. 1976)., **20**(18), pp. 1984–1988.

[11] Wilcox, R. K., Boerger, T. O., Hall, R. M., Barton, D. C., Limb, D., and Dickson, R. A., 2002, "Measurement of Canal Occlusion during the Thoracolumbar Burst Fracture Process," J. Biomech., **35**(3), pp. 381–384.

[12] Lehman, R. A., Paik, H., Eckel, T. T., Helgeson, M. D., Cooper, P. B., and Bellabarba, C., 2012, "Low Lumbar Burst Fractures: A Unique Fracture Mechanism Sustained in Our Current Overseas Conflicts," Spine J., **12**(9), pp. 784–790.

[13] Franklyn, M., and Stemper, B. D., 2017, "Military Injury Biomechanics: The Cause and Prevention of Impact Injuries," M. Franklyn, and P.V.S. Lee, eds., CRC Press, Boca Raton, FL.

[14] Wilcox, R. K., Boerger, T. O., Allen, D. J., Barton, D. C., Limb, D., Dickson, R. A., and Hall, R. M., 2003, "A Dynamic Study of Thoracolumbar Burst Fractures," J. Bone Joint Surg. Am., **85-A**, pp. 2184–2189.

[15] Zou, J., Yang, H., Miyazaki, M., Morishita, Y., Wei, F., McGovern, S., and Wang, J. C., 2009, "Dynamic Bulging of Intervertebral Discs in the Degenerative Lumbar Spine," Spine (Phila.

Pa. 1976)., **34**(23), pp. 2545–2550.

[16] Weishaupt, D., Schmid, M. R., Zanetti, M., Boos, N., Romanowski, B., Kissling, R. O., Dvorak, J., and Hodler, J., 2000, "Positional MR Imaging of the Lumbar Spine: Does It Demonstrate Nerve Root Compromise Not Visible at Conventional MR Imaging?," Radiology, **215**(1), pp. 247–253.

[17] Chung, S. S., Lee, C. S., Kim, S. H., Chung, M. W., and Ahn, J. M., 2000, "Effect of Low Back Posture on the Morphology of the Spinal Canal," Skeletal Radiol., **29**(4), pp. 217–223.

[18] Callaghan, J. P., and McGill, S. M., 2001, "Intervertebral Disc Herniation: Studies on a Porcine Model Exposed to Highly Repetitive Flexion/Extension Motion with Compressive Force," Clin. Biomech., **16**(1), pp. 28–37.

[19] Fujiwara, A., An, H. S., Lim, T. H., and Haughton, V. M., 2001, "Morphologic Changes in the Lumbar Intervertebral Foramen Due to Flexion-Extension, Lateral Bending, and Axial Rotation: An in Vitro Anatomic and Biomechanical Study," Spine (Phila. Pa. 1976)., **26**(8), pp. 876–882.

[20] Fradet, L., Arnoux, P. J., Ranjeva, J. P., Petit, Y., and Callot, V., 2014, "Morphometrics of the Entire Human Spinal Cord and Spinal Canal Measured from in Vivo High-Resolution Anatomical Magnetic Resonance Imaging," Spine (Phila. Pa. 1976)., **39**(4).

[21] Schmid, M. R., Stucki, G., Duewell, S., Wildermuth, S., Romanowski, B., and Hodler, J., 1999, "Changes in Cross-Sectional Measurements of the Spinal Canal and Intervertebral Foramina as a Function of Body Position: In Vivo Studies on an Open-Configuration MR System.," AJR. Am. J. Roentgenol., **172**(4), pp. 1095–1102.

[22] Lane, N. E., Nevitt, M. C., Genant, H. K., and Hochberg, M. C., 1993, "Reliability of New Indices of Radiographic Osteoarthritis of the Hand and Hip and Lumbar Disc Degeneration.," J. Rheumatol., **20**(11), pp. 1911–1918.

[23] Yoganandan, N., Pintar, F. A., Stemper, B. D., Baisden, J. L., Aktay, R., Shender, B. S., Paskoff, G., and Laud, P., 2006, "Trabecular Bone Density of Male Human Cervical and Lumbar Vertebrae," Bone, **39**(2), pp. 336–344.

[24] Van Toen, C., Street, J., Oxland, T. R., and Cripton, P. A., 2012, "Acoustic Emission Signals Can Discriminate between Compressive Bone Fractures and Tensile Ligament Injuries in the Spine during Dynamic Loading," J. Biomech., **45**(9), pp. 1643–1649.

[25] Reinhold, M., Audigé, L., Schnake, K. J., Bellabarba, C., Dai, L. Y., and Oner, F. C., 2013, "AO Spine Injury Classification System: A Revision Proposal for the Thoracic and Lumbar Spine," Eur. Spine J., **22**(10), pp. 2184–2201.

[26] Robinson, D. L., Tse, K. M., Franklyn, M., Zhang, J., Ackland, D., and Lee, P. V. S., 2019, "Cortical and Trabecular Bone Fracture Characterisation in the Vertebral Body Using Acoustic Emission," Ann Biomed Eng.

[27] Akoglu, H., 2018, "User's Guide to Correlation Coefficients," Turkish J. Emerg. Med., **18**(3), pp. 91–93.

[28] Tewari, M. K., Gifti, D. S., Singh, P., Khosla, V. K., Mathuriya, S. N., Gupta, S. K., and Pathak, A., 2005, "Diagnosis and Prognostication of Adult Spinal Cord Injury without Radiographic Abnormality Using Magnetic Resonance Imaging: Analysis of 40 Patients," Surg. Neurol., **63**(3), pp. 204–209.

[29] Sekhon, L. H. S., and Fehlings, M. G., 2001, "Epidemiology, Demographics, and Pathophysiology of Acute Spinal Cord Injury," Spine (Phila. Pa. 1976)., **26**(Supplement), pp. S2–S12.

[30] Boese, C. K., Müller, D., Bröer, R., Eysel, P., Krischek, B., Lehmann, H. C., and Lechler, P., 2016, "Spinal Cord Injury without Radiographic Abnormality (SCIWORA) in Adults: MRI Type Predicts Early Neurologic Outcome," Spinal Cord, **54**(10), pp. 878–883.

[31] Bogduk, N., 2005, *Clinical Anatomy of the Lumbar Spine and Sacrum*, Elsevier Health Sciences.

[32] Fagan, M. J., Julian, S., Siddall, D. J., and Mohsen, A. M., 2002, "Patient-Specific Spine Models. Part 1: Finite Element Analysis of the Lumbar Intervertebral Disc—a Material Sensitivity Study," Proc. Inst. Mech. Eng. Part H J. Eng. Med., **216**(5), pp. 299–314.

[33] Goel, V. K., Kong, W., Han, J. S., Weinstein, J. N., and Gilbertson, L. G., 1993, "A Combined Finite Element and Optimization Investigation of Lumbar Spine Mechanics with and without Muscles.," Spine (Phila. Pa. 1976)., **18**(11), pp. 1531–1541.

[34] Race, A., Broom, N. D., and Robertson, P., 2000, "Effect of Loading Rate and Hydration on the Mechanical Properties of the Disc," Spine (Phila. Pa. 1976)., **25**(6), pp. 662–669.

[35] van der Veen, A. J., Bisschop, A., Mullender, M. G., and van Dieën, J. H., 2013, "Modelling Creep Behaviour of the Human Intervertebral Disc," J. Biomech., **46**(12), pp. 2101–2103.

[36] Iatridis, J. C., Setton, L. A., Foster, R. J., Rawlins, B. A., Weidenbaum, M., and Mow, V. C., 1998, “Degeneration Affects the Anisotropic and Nonlinear Behaviors of Human Anulus Fibrosus in Compression,” J. Biomech., **31**(6), pp. 535–544.

[37] O’Connell, G. D., Vresilovic, E. J., and Elliott, D. M., 2011, “Human Intervertebral Disc Internal Strain in Compression: The Effect of Disc Region, Loading Position, and Degeneration,” J. Orthop. Res., **29**(4), pp. 547–555.

[38] Cassidy, J. J., Hiltner, A., and Baer, E., 1989, “Hierarchical Structure of the Intervertebral Disc,” Connect. Tissue Res., **23**(1), pp. 75–88.

[39] Fujita, Y., Duncan, N. A., and Lotz, J. C., 1997, “Radial Tensile Properties of the Lumbar Annulus Fibrosus Are Site and Degeneration Dependent,” J. Orthop. Res., **15**(6), pp. 814–819.

[40] Panjabi, M. M., Kifune, M., Wen, L., Arand, M., Oxland, T. R., Lin, R. M., Yoon, W. S., and Vasavada, A., 1995, “Dynamic Canal Encroachment during Thoracolumbar Burst Fractures.,” J. Spinal Disord., **8**(1), pp. 39–48.

[41] Yoganandan, N., Moore, J., Pintar, F. A., Banerjee, A., DeVogel, N., and Zhang, J., 2018, “Role of Disc Area and Trabecular Bone Density on Lumbar Spinal Column Fracture Risk Curves under Vertical Impact,” J. Biomech., **72**, pp. 90–98.

[42] Ochia, R. S., and Ching, R. P., 2002, “Internal Pressure Measurements during Burst Fracture Formation in Human Lumbar Vertebrae,” Spine (Phila. Pa. 1976)., **27**(11), pp. 1160–1167.

[43] Curry, W. H., Pintar, F. A., Doan, N. B., Nguyen, H. S., Eckardt, G., Baisden, J. L., Maiman, D. J., Paskoff, G. R., Shender, B. S., and Stemper, B. D., 2016, “Lumbar Spine Endplate Fractures: Biomechanical Evaluation and Clinical Considerations through Experimental Induction of Injury,” J. Orthop. Res., **34**(6), pp. 1084–1091.

[44] El Masri, F., Sapin de Brosses, E., Rhissassi, K., Skalli, W., and Mitton, D., 2012, “Apparent Young’s Modulus of Vertebral Cortico-Cancellous Bone Specimens,” Comput. Methods Biomech. Biomed. Engin., **15**(1), pp. 23–28.

[45] Yang, H., Jekir, M. G., Davis, M. W., and Keaveny, T. M., 2016, “Effective Modulus of the Human Intervertebral Disc and Its Effect on Vertebral Bone Stress,” J. Biomech., **49**(7), pp. 1134–1140.

[46] Stemper, B. D., Storvik, S. G., Yoganandan, N., Baisden, J. L., Fijalkowski, R. J., Pintar, F.

A., Shender, B. S., and Paskoff, G. R., 2011, “A New PMHS Model for Lumbar Spine Injuries during Vertical Acceleration.,” J. Biomech. Eng., **133**(8), p. 081002.

[47] Schönström, N., Lindahl, S., Willén, J., and Hansson, T., 1989, “Dynamic Changes in the Dimensions of the Lumbar Spinal Canal: An Experimental Study in Vitro,” J. Orthop. Res., **7**(1), pp. 115–121.

[48] Inufusa, A., An, H. S., Lim, T.-H., Hasegawa, T., Haughton, V. M., and Nowicki, B. H., 1996, “Anatomic Changes of the Spinal Canal and Intervertebral Foramen Associated with Flexion-Extension Movement,” Spine (Phila. Pa. 1976)., **21**(21), pp. 2412–2420.

[49] Alyas, F., Connell, D., and Saifuddin, A., 2008, “Upright Positional MRI of the Lumbar Spine,” Clin. Radiol., **63**(9), pp. 1035–1048.

[50] Jinkins, J. R., Dworkin, J. S., and Damadian, R. V., 2005, “Upright, Weight-Bearing, Dynamic-Kinetic MRI of the Spine: Initial Results,” Eur. Radiol., **15**(9), pp. 1815–1825.

Tables

Table 1: Descriptive characteristics for the cadavers corresponding to the three-vertebrae specimens used in the mechanical testing. For the corresponding three-vertebrae specimen, the vBMD of the center vertebra, intervertebral disc grading, and number of specimens with Schmorls nodes are indicated.

Combination	Number of specimens	Age (yrs)	Total height (cm)	Total weight (kg)	BMI (kg/m^2)	vBMD (mg/cm^3)	Intervertebral disc grading	Number of specimens with Schmorls nodes
T12-L1-L2	2	62.5±2.1	183.0±0.0	91.0±9.9	27.2±3.0	136.3±43.2	1.0±0.0	1
L1-L2-L3	4	61.0±12.5	180.0±17.9	84.8±25.6	25.5±3.1	154.5±24.2	0.5±1.0	2
L2-L3-L4	5	65.6±10.7	171.4±3.4	83.3±24.0	27.9±13.7	166.3±72.8	1.2±0.8	4
L3-L4-L5	5	57.4±7.8	177.6±6.4	80.9±37.4	23.5±6.0	171.6±56.1	1.0±0.7	0
L4-L5-S1	4	60.3±12.1	186.3±10.4	74.4±20.1	26.3±2.2	165.5±71.5	1.0±1.2	1
Total	20	61.3±9.7	178.8±10.4	83.3±24.0	25.9±7.2	162.1±53.7	1.0±0.8	8

BMI, Body mass index; vBMD, volumetric bone mineral density of vertebral body trabecular bone; Intervertebral disc grading, grading of the more severely degraded intervertebral disc of each three-vertebrae specimen according to clinical radiographic criteria [22].

Table 2: Specimen-specific attributes (mean±1SD) related to geometry, rigidity and vBMD of three-vertebrae lumbar spine specimens with compression tests of each fracture category.

	Three-vertebra specimen	n	a_{VB} (cm^2)	a_{IVD} (cm^2)	$a_{canal,i}$ (pixels)	h_{VB} (mm)	h_{VB+IVD} (mm)	vBMD (mg/cm^3)	Intervertebral disc grading	Number of specimen with Schmorls nodes
Non-fracture	T12-L1-L2	2	12.2±1.7	18.3±2.0	12007.0±878.2	26.7±1.4	35.9±1.4	144.6±46.8	1.0±0.0	1
	L1-L2-L3	4	12.9±0.9	22.0±2.9	5422.3±1876.6	29.8±3.3	39.2±2.9	165.8±34.7	0.5±1.0	2
	L2-L3-L4	3	14.0±0.7	22.5±2.9	4207.0±1734.0	29.4±0.9	38.9±2.1	138.0±62.8	1.0±1.0	2
	L3-L4-L5	6	15.3±1.2	21.5±1.4	5369.0±696.3	28.7±1.4	39.4±0.4	244.6±109.7	1.2±0.4	0
	L4-L5-S1	4	14.9±0.7	22.9±1.7	756.3±378.5	31.9±2.3	38.8±1.2	194.8±120.7	1.0±1.2	1
	Total	19	14.2±1.5	21.7±2.3	4425.6±4775.9	29.5±2.4	38.8±1.8	190.2±91.4	0.9±0.8	6
Fracture	T12-L1-L2	2	12.2±1.7	18.3±2.0	10858.5±870.4	26.7±1.4	35.9±1.4	144.6±46.8	1.0±0.0	1
	L1-L2-L3	4	12.9±0.9	22.0±2.9	4977.0±2577.4	29.8±3.3	39.2±2.9	165.8±34.7	0.5±1.0	2
	L2-L3-L4	5	14.4±1.2	23.6±3.1	3843.8±1842.1	29.1±1.6	36.7±4.6	195.9±112.1	1.2±0.8	4
	L3-L4-L5	3	14.6±1.5	20.6±1.5	4032.0±2101.5	29.0±0.6	39.3±0.6	146.2±18.0	1.0±1.0	0
	L4-L5-S1	4	14.9±0.7	22.9±1.7	833.8±509.4	31.9±2.3	38.8±1.2	194.8±120.7	1.0±1.2	1
	Total	18	14.0±1.4	22.0±2.8	4930.4±4948.4	29.6±2.4	38.1±2.9	175.0±80.0	0.9±0.9	8

a_{VB} and a_{IVD}, cross-sectional areas at the mid-plane of the vertebral body and intervertebral disc, respectively; $a_{canal,i}$, area of the spinal canal prior to mechanical testing; h_{VB}, height of the vertebral body of the center vertebrae; h_{VB+IVD}, height of the vertebral body of the center vertebrae and the lower intervertebral disc; vBMD, volumetric bone mineral density; Intervertebral disc grading, grading of the more severely degraded intervertebral disc of each three-vertebrae specimen according to clinical radiographic criteria [22].

Table 3: Pearson's correlation coefficient (R) (mean±1SD) between canal occlusion and compressive force or displacement up to the point of maximum occlusion or for the entire compression experiment. Variables are calculated for specimens of all lumbar levels for each fracture category.

Interval	Outcome variable	Explanatory variable	Correlation coefficient (R)	
			Non-fracture	Fracture
t=0 to $t_{max,o}$	O_{canal}	d_z	0.93±0.13***	0.95±0.04***
		F_z	0.78±0.28***	0.93±0.05***
t = 0 to 2s	O_{canal}	d_z	0.86±0.41***	0.83±0.22***
		F_z	0.83±0.34***	0.71±0.28***

O_{canal}, spinal canal occlusion; d_z, displacement; F_z, compressive force; $t_{max,o}$, time corresponding to maximum occlusion

***p<0.001

Table 4: Occlusion and compressive variables (mean±1SD) obtained for each fracture group.

Group	Three vertebra specimen	n	Number of tests per specimen	$\varepsilon_{z,max}$ *(%)*	$d_{z,max}$ (mm)	$F_{z,max}$ (N)	O_{max} (%)	O_{final} (%)
Non-fracture	T12-L1-L2	2	2.5±0.7	10.0±6.3	3.6±2.1	2325.9±938.2	18.1±0.4	0.0±0.0
	L1-L2-L3	4	3.0±1.4	9.7±2.3	3.8±1.0	5425.6±1632.2	57.8±49.2	0.6±1.0
	L2-L3-L4	3	2.3±0.6	8.8±3.2	4.0±1.2	4866.1±2539.6	27.5±45.4	0.6±0.5
	L3-L4-L5	6	2.8±1.2	9.4±6.2	3.3±2.0	3624.7±3469.7	58.8±31.1	0.5±1.2*
	L4-L5-S1	4	2.3±0.5	9.5±1.1*	3.7±0.3*	6818.2±2470.3	31.3±12.4	5.3±10.7
	All	19	2.6±1.0	9.4±3.5***	3.6±1.3***	4866.1±2631.7	43.6±34.6	1.5±4.9*
Fracture	T12-L1-L2	2	3.5±0.7	16.0±5.8	5.7±1.9	2259.5±1203.3	26.6±10.4	6.8±4.6
	L1-L2-L3	4	4.8±2.4	18.5±7.5	7.4±3.4	6971±3207.1	21.5±13.5	8.5±11.0
	L2-L3-L4	5	2.8±0.8	14.9±3.9	5.5±1.9	7014.4±2498.8	48.6±27.9	0.9±2.0
	L3-L4-L5	3	2.3±0.6	15.1±1.1	6.0±0.3	6249.2±2670.6	61.2±39.7	77.7±38.6*
	L4-L5-S1	4	3.3±0.5	12.3±1.6*	4.8±0.6*	6620±1205.6	56.1±47.5	12.0±14.2
	All	18	3.3±1.4	15.3±4.6***	5.9±2.0***	6261.2±2581.6	43.9±32.5	18.5±31.5*

n, number of specimens; $d_{z,max}$, displacement at maximum occlusion ; $F_{z,max}$ maximum axial compressive force; O_{max}, maximum occlusion; O_{final}, final occlusion;
* $p<0.05$.
*** $p<0.001$

Table 5: Occlusion and compressive variables (mean±1SD) obtained for the tests identified with isolated trabecular fractures or combined cortical and trabecular fractures.

Fracture type	Three vertebra specimen	n	Number of tests per specimen	$\varepsilon_{z,max}$ *(%)*	$d_{z,max}$ (mm)	$F_{z,max}$ (N)	O_{max} (%)	O_{final} (%)
Isolated trabecular fracture	T12-L1-L2	1	4.0	20.1±0.0	7.0±0.0	3110.4±0.0	19.3±0.0	3.6±0.0
	L1-L2-L3	1	5.0	21.6±0.0	7.8±0.0	6899.3±0.0	27.7±0.0	10.6±0.0
	L2-L3-L4	1	2.0	15.2±0.0	4.4±0.0	11038.7±0.0	71.3±0.0	0.0±0.0
	L3-L4-L5	0	0.0±0.0	0.0±0.0	0.0±0.0	0.0±0.0	0.0±0.0	0.0±0.0
	L4-L5-S1	2	3.5±0.7	12.9±2.5	4.9±1.0	6982.5±1896.8	56.6±53.3	13.9±19.6
	All	5	3.6±1.1	16.5±4.3	5.8±1.6	7002.7±2960.1	46.3±34.5	8.4±11.6
Combined cortical and trabecular fracture	T12-L1-L2	1	3.0±0.0	11.9±0.0	4.4±0.0	1408.6±0.0	34.0±0.0	10.0±0.0
	L1-L2-L3	3	4.7±2.9	17.5±8.8	7.2±4.1	6994.9±3927.5	19.4±15.8	7.7±13.4
	L2-L3-L4	4	3.0±0.8	14.9±4.5	5.8±2.0	6008.3±1255.9	43.0±28.8	1.2±2.3
	L3-L4-L5	3	2.3±0.6	15.1±1.1	5.9±0.3	6249.2±2670.6	61.2±39.7	77.7±38.6
	L4-L5-S1	2	3.0±0.0	11.7±0.7	4.7±0.4	6257.5±486.2	55.7±62.6	10.1±14.2
	All	13	3.2±1.5	14.8±4.7	5.9±2.2	5976.1±2490.7	43.0±33.1	22.4±36.1

n, number of specimens; $d_{z,max}$, displacement at maximum occlusion ; $F_{z,max}$ maximum axial compressive force; O_{max}, maximum occlusion; O_{final}, final occlusion;

Table 6: Stepwise multiple linear regression results describing the dependencies of the occlusion variables.

Outcome variable	Step	Included predictor variables	R	B	β	p-value	Tolerance	VIF	Excluded predictor variables (corresponding p-value)
O_{max}	1	Constant	0.57**	-2.61		0.832			$d_{z,max}$ (<0.001)
		Lumbar level		14.29	0.57	<0.001	1.00	1.00	$\varepsilon_{z,max}$ (<0.001)
									a_{VB} (0.036)
									a_{IVD} (0.063)
									$a_{canal,i}$ (0.247)
									h_{VB} (0.921)
									h_{VB+IVD} (0.425)
									vBMD (0.595)
									Fracture status (0.997)
									Schmorl's nodes (0.900)
									Intervertebral disc grading (0.980)
	2	Constant	0.79**	-55.00		<0.001			$\varepsilon_{z,max}$ (0.909)
		Lumbar level		17.05	0.68	<0.001	0.96	1.04	a_{VB} (0.031)
		$d_{z,max}$		9.22	0.56	<0.001	0.96	1.04	a_{IVD} (0.159)
									$a_{canal,i}$ (0.340)
									h_{VB} (0.429)
									h_{VB+IVD} (0.888)
									vBMD (0.123)
									Fracture status (0.331)
									Schmorl's nodes (0.798)
									Intervertebral disc grading (0.330)

	3	Constant	0.82**	31.79		0.438			$\varepsilon_{z,max}$ (0.932)
		Lumbar level		22.28	0.89	<0.001	0.52	1.91	a_{IVD} (0.463)
		$d_{z,max}$		8.77	0.53	<0.001	0.95	1.06	$a_{canal,i}$ (0.197)
		a_{VB}		-0.07	-0.31	0.031	0.52	1.92	h_{VB} (0.335)
									h_{VB+IVD} (0.775)
									vBMD (0.284)
									Fracture status (0.275)
									Schmorl's nodes (0.923)
									Intervertebral disc grading (0.653)
O_{final}	1	Constant	0.37*	1.51		0.770			$d_{z,max}$ (0.592)
		Fracture status		17.00	0.37	0.026	1.00	1.00	$\varepsilon_{z,max}$ (0.775)
									a_{VB} (0.307)
									a_{IVD} (0.499)
									a_{canal} (0.483)
									h_{VB} (0.928)
									h_{VB+IVD} (0.228)
									vBMD (0.775)
									Schmorl's nodes (0.158)
									Intervertebral disc grading (0.640)

O_{max}, maximum occlusion; O_{final}, final occlusion; Lumbar level, level along lumbar spine of center vertebra; $d_{z,max}$, displacement at maximum occlusion; $\varepsilon_{z,max}$, compressive strain at maximum occlusion, a_{VB}, cross-sectional area at the mid-plane of the vertebral body; $a_{canal,i}$, initial canal area; a_{IVD}, cross-section area cross-sectional area at the mid-plane of the lower intervertebral disc; $h_{VB,}$ height of the vertebral body of the center vertebrae; $h_{VB+IVD,}$ height of the vertebral body of the center vertebrae and the lower intervertebral disc; vBMD, volumetric bone mineral density; Fracture status, categorical variable denoting a test with no fracture or a fracture as 0.0 and 1.0, respectively; Schmorl's nodes, categorical variable denoting absence or presence of Schmorl's nodes as 0.0 and 1.0, respectively; Intervertebral disc grading, grading of the more severely degraded intervertebral disc of each three-vertebrae specimen according to clinical radiographic criteria [22].R, Pearson's correlation coefficient; B, B-coefficient representing regression slope between predictor and outcome variable; β, standardized B-coefficient; VIF, variance inflation facture.

Figure captions

Fig. 1: Geometric parameters describing specimen size from the CT images. **(a)** Sagittal view of three-vertebrae specimen, depicting the mid-planes of the center vertebral body and the caudal intervertebral disc (yellow and red dashed lines, respectively), the height of the vertebral body (h_{VB}), and the combined height of the center vertebral body and caudal intervertebral disc (h_{VB+IVD}). **(b)** Axial view of mid-plane of the center vertebral body from which its corresponding area (a_{VB}) was measured, as indicated by the yellow line. **(c)** Axial view of mid-plane of the caudal intervertebral disc, from which its corresponding area (a_{IVD}) was measured, as indicated by the red line.

Fig. 2: Schematic of mechanical testing method. Each specimen was tested in a loading sequence that comprised preloading of 5 cycles at 1 Hz from 0 to 0.1 mm of compression, dynamic loading at the maximum acceleration of the testing machine to a 4% interval of axial strain (ε_z), unloaded over a 1 second interval, then allowed to recover unloaded for approximately 30 minutes. The loading sequence was repeated in increments of 4% increase in ε_z until a fracture was detected. The dynamic loading data from the final test was assigned to the fracture group, whilst the dynamic loading data from the second last test was assigned to the non-fracture group.

Fig. 3: Schematic of instrumentation and mechanical testing setup. The frontal view of the center vertebra depicts the position of the left and right AE sensors and the sagittal view of three-vertebrae specimen depicts the measurement of the spinal canal occlusion. Light generated from the cold light source travels anteriorly and is reflected downwards by a 45-degree mirror through the spinal

canal. The light is then reflected by a second 45-degree mirror and travels posteriorly to a high-speed camera.

Fig. 4: Plots demonstrating occlusion and compression variables obtained from each compression test. (**a)** Spinal occlusion measurements obtained for the entire two seconds of the compression test. From Time = 0 ms, the specimen was dynamically compressed to a specified amount of displacement. The compression was subsequently removed over the next 1000 ms, then remained unloaded for 1000 ms. The final occlusion (O_{final}) was obtained at 2000 ms. The initial region of dynamic loading (black dashed line) was considered for further analysis. **(b)** Close-up view of occlusion measurements during dynamic compression. The dashed black lines indicate the point of maximum occlusion (O_{max}). **(c)** Compressive force during dynamic compression. The force at maximum occlusion ($F_{z,max}$) is shown. **(d)** Compressive displacement during the dynamic compression. The displacement at maximum occlusion ($d_{z,max}$) is indicated.

Fig. 5: Occlusion and compressive force measurements obtained during dynamic compression for a representative specimen at each lumbar level. Data represent measurements from -20 ms to 60 ms, relative to the start of dynamic compression (Time = 0 ms). Images depict the high-speed camera view at the time points: prior to compression (0 ms), maximum occlusion (O_{max}), and shortly after maximum occlusion (50 ms). The anterior (a) and posterior (p) directions are indicated.

Fig. 1

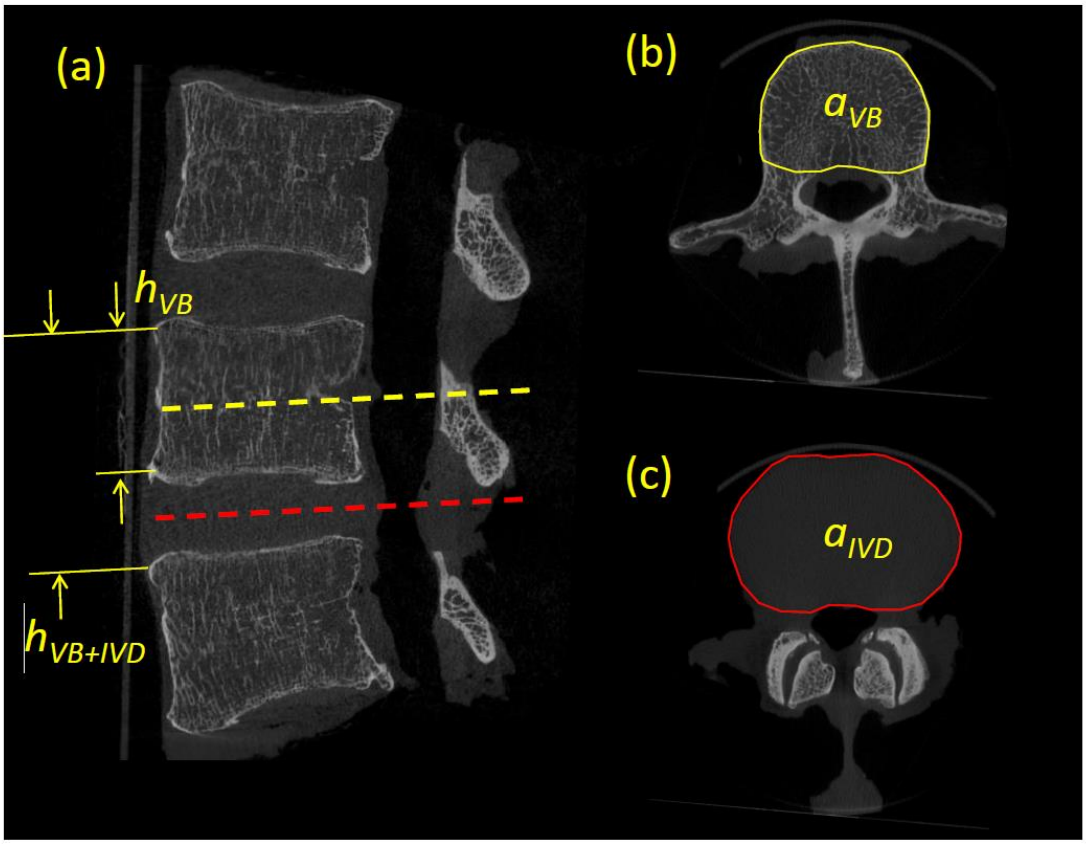

Fig. 2

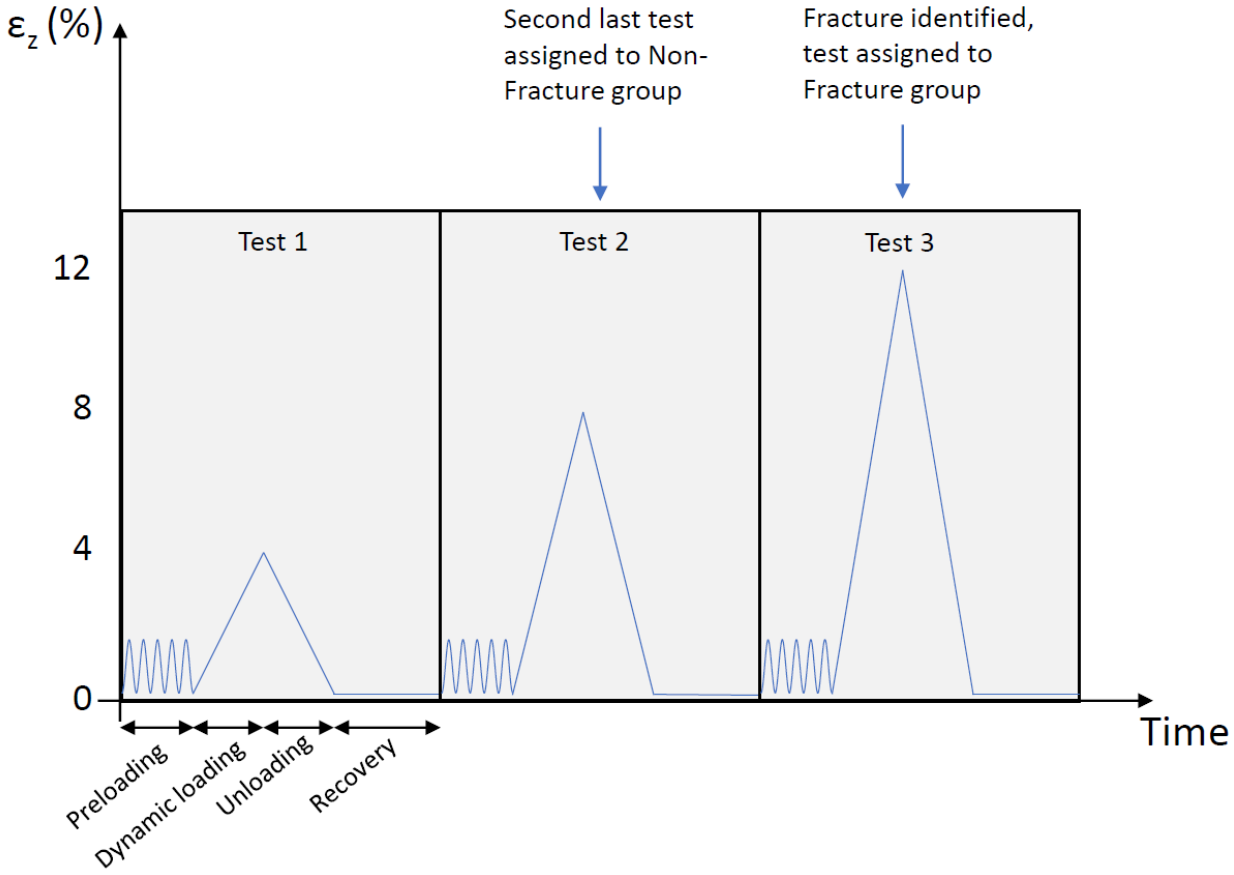
ε_z (%)
Second last test assigned to Non-Fracture group
Fracture identified, test assigned to Fracture group
Test 1
Test 2
Test 3
12
8
4
0
Time
Preloading
Dynamic loading
Unloading
Recovery

Fig. 3

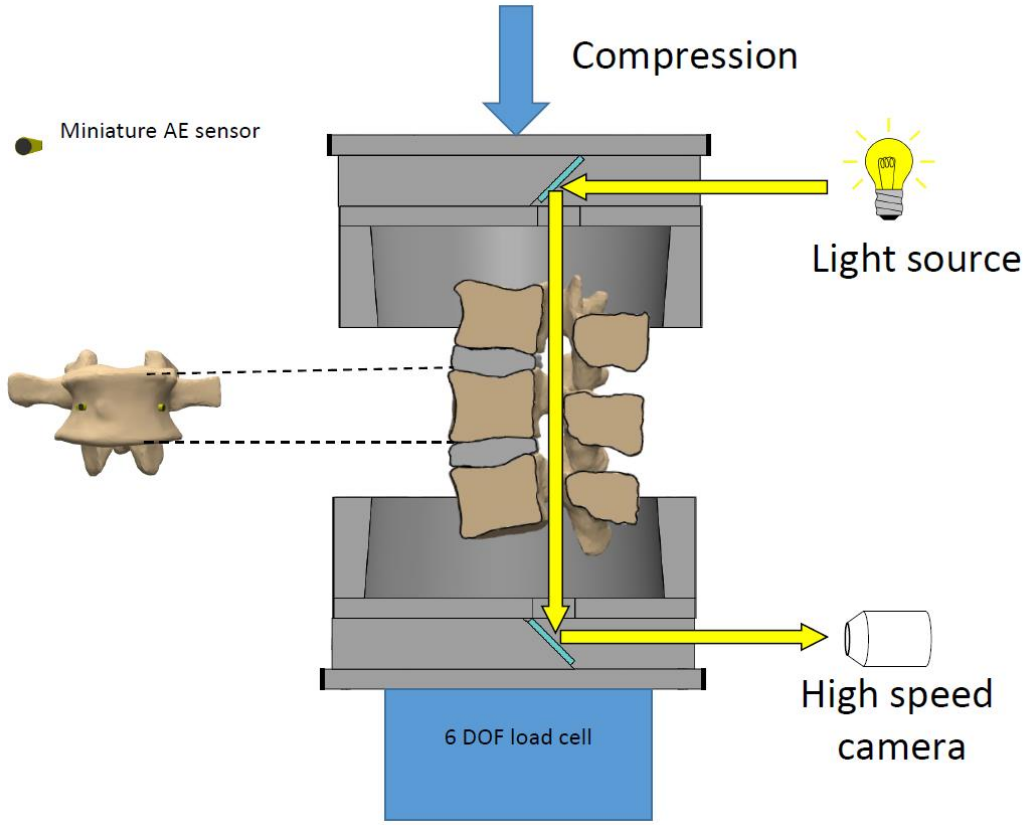
Compression
Miniature AE sensor
Light source
High speed
camera
6 DOF load cell

Fig. 4

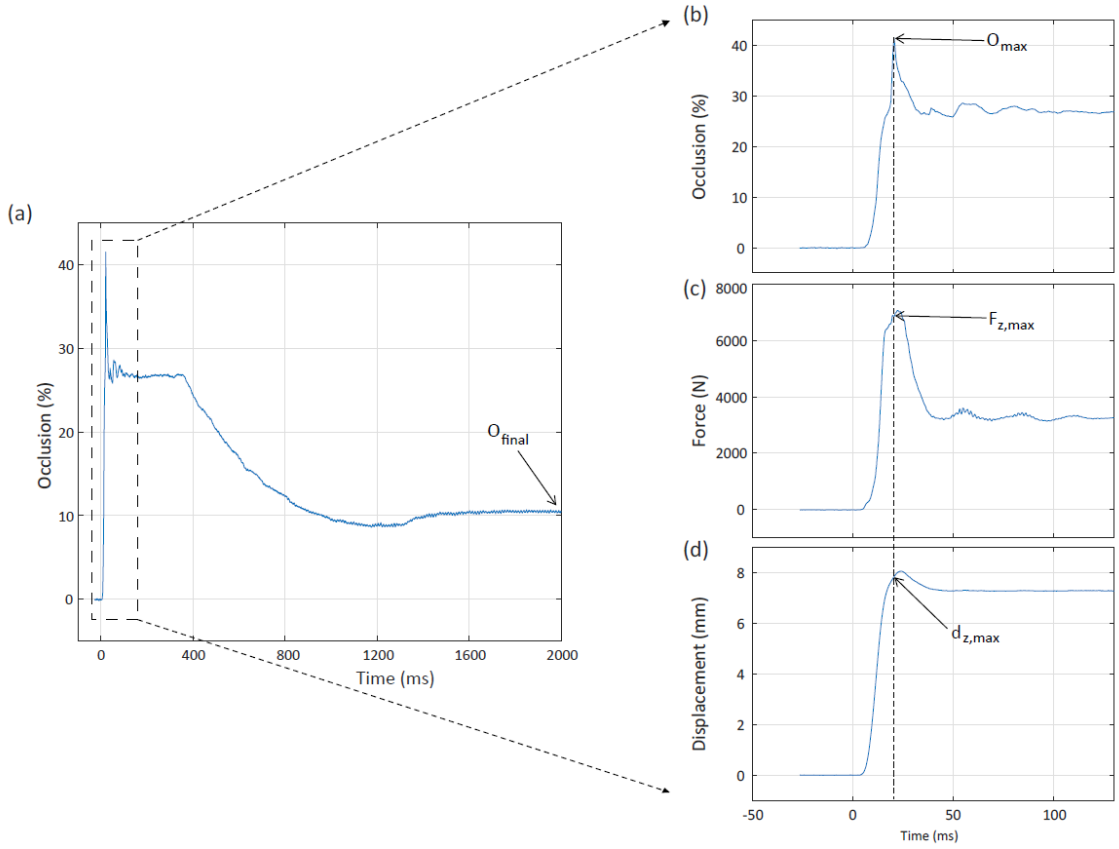
(a)
Occlusion (%)
Time (ms)
O_{final}
(b)
Occlusion (%)
O_{max}
(c)
Force (N)
$F_{z,max}$
(d)
Displacement (mm)
$d_{z,max}$
Time (ms)

Fig. 5

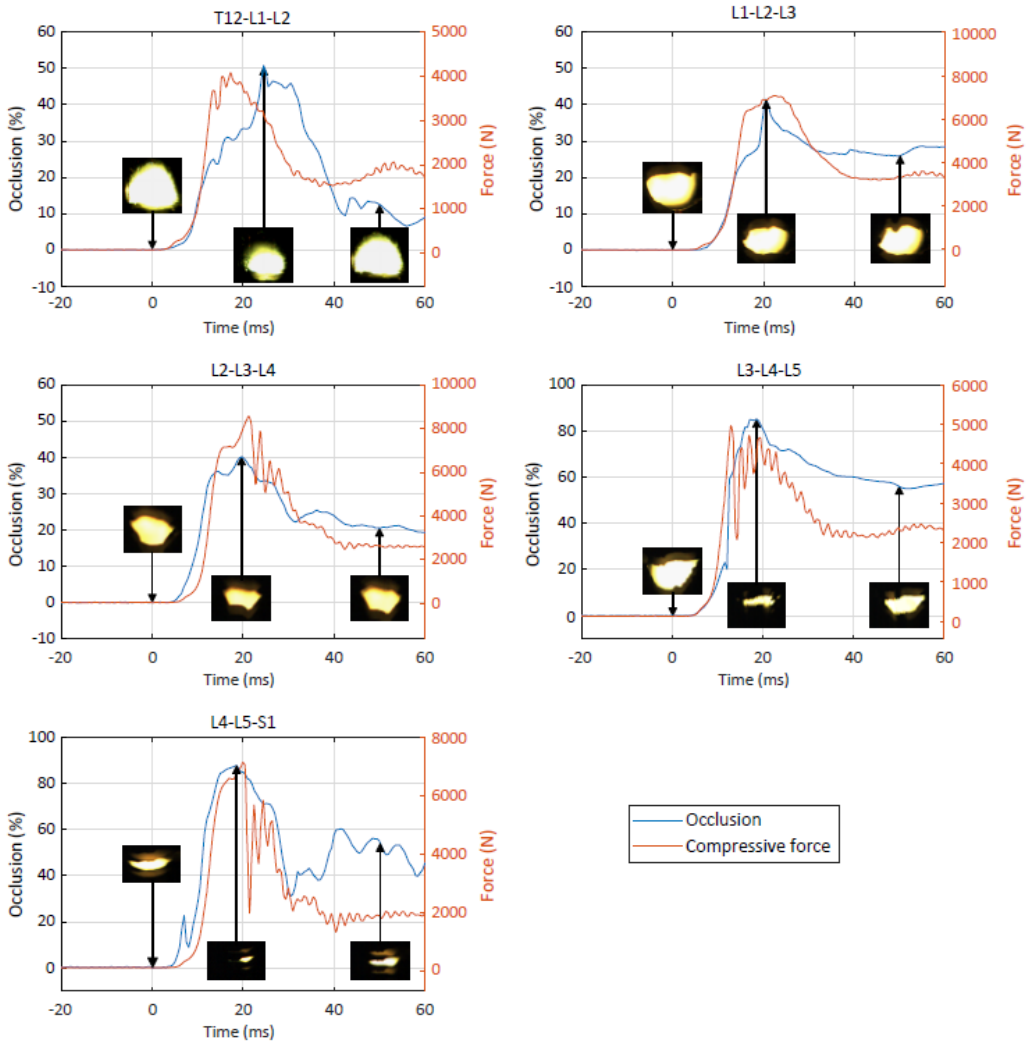
T12-L1-L2
L1-L2-L3
L2-L3-L4
L3-L4-L5
L4-L5-S1
Occlusion (%)
Force (N)
Time (ms)
Occlusion
Compressive force